

Geometallurgical and Kinetic Controls on Cyanidation of a Mildly Refractory Low-Sulfidation Epithermal Gold Ore: Insights from the Mount Muro System, Indonesia

Frideni Yushandiana Putri G.F.^{1*}, Nizar Angga Kusuma², Ronny Winarko³, and Adinda Dwi Nugraheni¹

¹Department of Mining Engineering, Metallurgical Engineering Program, Universitas Pembangunan Nasional “Veteran” Yogyakarta, Indonesia 55283

²Cikondang Kencana Prima (CKP) Gold Mine, Cianjur, West Java, Indonesia 43263

³Hazen Research Inc., 4601 Indiana Street, Golden, Colorado, USA, 80403

Abstract. Gold (Au) and silver (Ag) are commonly co-extracted from low-sulphidation epithermal (LSE) ores by alkaline cyanidation, yet their dissolution behaviors often diverge despite close mineralogical association. This study investigates Au–Ag cyanidation in ore from the Mount Muro LSE deposit, Central Kalimantan, Indonesia, through integrated mineralogical characterization, diagnostic leaching, time-resolved cyanidation, residue analysis, and kinetic modeling. Diagnostic leaching indicates that ~80% of Au is cyanide-accessible at $P_{80} \approx 75 \mu\text{m}$, whereas only ~54% of Ag occurs in free-milling domains, with the remainder hosted in sulfide and Cu–Ag sulfosalt phases. Continuous cyanidation confirms this contrast: Au dissolves rapidly and reaches a plateau of ~87% recovery, while Ag extraction proceeds more gradually to ~78%. Residue analysis shows that unrecovered Au and Ag are concentrated in fine fractions (<38 μm), demonstrating control by mineralogical locking, partial passivation, and micro-scale diffusional barriers rather than reagent insufficiency. Shrinking Core Model diagnosis identifies mixed kinetic control for Au and diffusion-dominated control for Ag. Despite differing dominant mechanisms, kinetic model discrimination shows that both metals are best described by the Ling model, capturing non-linear, accessibility-controlled dissolution. These results highlight evolving surface accessibility as the primary control on cyanidation performance in mildly refractory LSE ores.

1 Introduction

Gold extraction from mineral ores remains one of the most persistent challenges in mineral processing, owing to the wide variability in gold occurrence and the strong dependence of leaching performance on ore mineralogy and effective surface accessibility. Gold exhibits exceptional physical and chemical properties, including high corrosion resistance, chemical inertness, electrical conductivity, and biocompatibility, which underpin its extensive applications in jewelry, electronics, catalysis, and medical technologies. These same properties, however, confer intrinsically low chemical reactivity under many processing conditions, rendering gold extraction highly sensitive not only to chemical feasibility, but to the mineralogical context and the progressive evolution of reactive surface area during hydrometallurgical treatment.

In natural geological systems, gold does not occur as a single uniform phase, but rather spans a broad spectrum of physical forms, from liberated coarse grains to fine and submicron inclusions hosted within sulfide, sulfosalt, or silicate minerals. Ore microscopy and metallurgical investigations consistently demonstrate that gold department and host mineralogy exert first-order control on cyanidation performance [1]. Free or

partially exposed native gold and electrum typically dissolve readily under alkaline cyanide conditions, whereas gold associated with sulfides, sulfosalts, or silicate matrices often exhibits slower dissolution kinetics and incomplete recovery, even under fine grinding and reagent-sufficient conditions [2]. These observations underscore that cyanidation efficiency is governed less by thermodynamic feasibility than by the accessibility of gold-bearing surfaces to reactive species.

Low-sulfidation epithermal (LSE) gold deposits constitute one of the most economically significant classes of precious-metal systems worldwide. These deposits form from near-neutral to mildly alkaline hydrothermal fluids under relatively low sulfur fugacity and are commonly characterized by quartz–carbonate \pm adularia gangue assemblages [3], [4]. Well-developed open-space filling textures, including banded, crustiform, and cockade veins, are typical of LSE systems and are often associated with free-milling gold [5]. Consequently, LSE deposits are frequently regarded as metallurgically straightforward.

However, increasing mineralogical evidence demonstrates that not all gold in LSE systems occurs in uniformly liberated or reactive forms. A significant proportion of gold may occur as fine inclusions within

* Corresponding author: frideni_gf@yahoo.com

sulfide minerals such as pyrite, sphalerite, and chalcopyrite, or be associated with sulfosalt phases including tetrahedrite–tennantite, as well as dispersed within hydrothermally altered silicate matrices [1], [6]. Although the overall sulfide content of LSE ores is generally low, these textural and mineralogical associations impose intrinsic constraints on effective surface accessibility and contribute to mildly refractory behavior. As a result, LSE ores commonly exhibit rapid initial extraction followed by premature recovery plateaus, reflecting progressive loss of accessible reactive surfaces rather than exhaustion of chemical driving force.

Cyanidation remains the dominant hydrometallurgical method for gold extraction due to its high selectivity and effectiveness under alkaline conditions. Gold and silver dissolution proceeds according to the Elsner reactions, requiring both free cyanide and dissolved oxygen to sustain reaction progress [2]. In practice, however, cyanidation performance is frequently governed not by reagent availability, but by mineralogical and surface-related constraints that limit the transport of cyanide and oxygen to metal-bearing interfaces. Preferential oxidation of sulfide and sulfosalt phases, and the subsequent formation of passivating surface layers, such as elemental sulfur, iron oxyhydroxides, or copper-bearing products, can progressively reduce effective reaction rates during leaching, particularly in ores containing reactive sulfide and Cu-bearing minerals [2]. These processes highlight the need to distinguish clearly between reagent sufficiency and accessibility-controlled kinetic limitation.

Geometallurgical approaches provide a powerful framework for integrating geological, mineralogical, and metallurgical information to predict processing behavior and variability across an orebody [7], [8]. Within LSE systems, variations in mineral assemblages, ore textures, and precious-metal deportment reflect vertical and lateral zonation linked to hydrothermal fluid evolution and boiling processes [4], [5]. These geological controls ultimately govern gold liberation, surface accessibility, reagent consumption, and time-dependent leaching response, emphasizing the importance of explicitly linking ore-forming processes with hydrometallurgical performance.

The Mount Muro gold district in Central Kalimantan, Indonesia, represents a well-documented example of a low-sulfidation epithermal system characterized by complex alteration patterns and diverse ore textures. Geological studies describe extensive silicification, argillic, propylitic, and sericitic alteration, with gold mineralization hosted in quartz–carbonate veins displaying banded and cockade textures. Mineralogical investigations indicate that gold occurs predominantly as native gold and electrum, accompanied by variable associations with sulfide and sulfosalt minerals reflecting transitions between precious-metal-rich and base-metal-rich domains [9]. While this geological framework is well established, the metallurgical consequences of such mineralogical heterogeneity, particularly in terms of gold deportment,

time-dependent leaching kinetics, and surface evolution during cyanidation, remain insufficiently constrained.

Although cyanidation of epithermal gold ores has been widely investigated, relatively few studies have systematically integrated diagnostic leaching, detailed mineralogical characterization, and time-resolved kinetic modeling to elucidate the mechanisms governing recovery limitation in mildly refractory LSE systems. Diagnostic leaching enables quantitative assessment of gold distribution among operationally defined accessibility domains, while kinetic modeling provides insight into the relative roles of surface reaction and mass transport processes during leaching [1]. Integrating these approaches offers a robust pathway to distinguish between chemical feasibility and accessibility-controlled kinetic behavior.

Accordingly, this study investigates the cyanidation kinetics and geometallurgical behavior of a mildly refractory low-sulfidation epithermal gold ore from the Mount Muro system. By combining fine grinding, oxidant-assisted cyanidation, diagnostic leaching, residue characterization, and time-resolved kinetic modeling, this work aims to clarify how gold deportment, mineralogical locking, and the progressive evolution of effective surface accessibility govern extraction efficiency. The results provide new insight into accessibility-controlled cyanidation in epithermal gold systems and establish a mechanistic foundation for interpreting time-dependent leaching behavior in ores exhibiting subtle but economically significant refractory characteristics

2 Research methods

2.1 Geological and mineralogical secondary data compilation

Secondary geological and mineralogical data for the Mount Muro low-sulfidation epithermal (LSE) system were compiled from previously published, peer-reviewed studies [9], [10], [11]. These sources provide validated descriptions of hydrothermal alteration assemblages, vein textures, primary ore mineral associations, paragenetic sequences, and paleo-hydrothermal fluid characteristics, including fluid inclusion assemblages (FIAs), homogenization temperatures (Th), and salinity ranges.

The compiled datasets were used exclusively to support geometallurgical interpretation, with specific emphasis on identifying mineralogical and textural controls on gold and silver deportment and on the accessibility of reactive surfaces during cyanidation. Parameters extracted from the literature include alteration styles, vein and ore textures, primary sulfide and sulfosalt minerals associated with Au–Ag mineralization, and fluid inclusion characteristics indicative of deep boiling and evolving hydrothermal conditions.

Mineralogical interpretation in this study is restricted to ore-formation context and textural association analysis, consistent with established principles of reflected-light microscopy and epithermal

ore characterization [1]. No reinterpretation of primary geological datasets was attempted. Secondary data usage was confined to peer-reviewed publications to ensure interpretive robustness and to maintain clear separation between literature-derived geological context and experimentally generated metallurgical data.

2.2 Materials and ore preparation

Bulk gold-bearing ore samples were collected from mineralized zones of the Mount Muro mining district, Central Kalimantan, Indonesia. The deposit is classified as a low-sulfidation epithermal system based on alteration mineralogy, vein textures, and fluid inclusion characteristics reported in previous studies [9].

To ensure feed representativeness and minimize size- and density-related segregation effects, the bulk ore was homogenized using standard coning and quartering procedures, followed by rotary sample division to produce mass-balanced sub-samples for metallurgical testing.

Comminution was conducted using a laboratory-scale ball mill in accordance with standard mineral-processing practice. Two target grind sizes were prepared to meet distinct experimental objectives. A grind size of $P_{80} \approx 75 \mu\text{m}$ was selected for diagnostic leaching tests to align with common industrial benchmarking and comparative studies. A finer grind size of $P_{80} \approx 54 \mu\text{m}$ was prepared for kinetic experiments to enhance mineral liberation and to increase sensitivity to intrinsic dissolution behavior, while maintaining particle-scale conditions representative of practical cyanidation systems.

2.3 Chemical digestion and elemental quantification

Gold (Au) and silver (Ag) contents in solid samples were determined by lead-collection fire assay followed by cupellation, which remains the reference method for total precious-metal determination in siliceous and sulfide-bearing ores due to its robustness against gangue-related analytical interference [1], [2]. The resulting doré beads were dissolved in aqua regia to quantitatively transfer precious metals into solution prior to instrumental analysis.

Copper (Cu) contents in solid samples were determined by direct aqua regia digestion of the leach feed. This approach preferentially dissolves Cu from sulfide and oxide phases that are chemically and kinetically relevant under cyanidation conditions, while avoiding HF-based silicate decomposition. Accordingly, the measured Cu concentrations reflect reagent-accessible Cu behavior pertinent to cyanidation environments rather than total lattice-bound Cu in silicate minerals.

All dissolved metal concentrations were measured using flame atomic absorption spectrometry (AAS; Agilent Varian 77). Analytical reliability was verified through duplicate and triplicate analyses of both solid and solution samples. Relative analytical uncertainty was maintained below 5% at the 95% confidence level,

consistent with accepted QA/QC thresholds for metallurgical and kinetic studies. These controls ensure that subsequent interpretation of extraction behavior and kinetics reflects intrinsic ore response rather than analytical or preparation-related artifacts.

2.4 Diagnostic leaching for gold deportment inference

Diagnostic leaching was conducted on the homogenized ore feed ground to $P_{80} \approx 75 \mu\text{m}$ to infer the mineralogical deportment of gold (Au), silver (Ag), and copper (Cu) across operationally defined accessibility domains characteristic of the Mount Muro low-sulphidation epithermal (LSE) system [9]. This grind size was selected to align with common industrial liberation benchmarks [2], enabling discrimination of metal-hosting domains while avoiding excessive liberation artefacts associated with ultra-fine grinding.

A five-stage sequential dissolution protocol was applied to interrogate these accessibility domains, as summarized in Table 1. The procedure commenced with alkaline cyanidation (Stage 1) to quantify the free-milling and readily accessible precious-metal fraction. This was followed by nitric acid digestion and subsequent cyanide re-leaching (Stages 2–3), designed to access metals associated with acid-labile sulfides and reactive sulfide matrices, including inclusions not directly exposed during initial cyanidation. Finally, aqua regia digestion and fire assay (Stages 4–5) were employed to quantify the residual metal inventory associated with relatively inert sulfides and refractory silicate or carbonate matrices.

Table 1. Summary of Diagnostic Leaching Procedure for Low-Sulfidation Epithermal Gold Ores

Stage	Main Reagent / Condition	Target Mineral Phase
1. Cyanide Amenability	NaCN solution, pH \approx 10.5	Exposed native gold and electrum (Au–Ag alloy) associated with quartz–adularia gangue
2. Nitric Acid Digestion	HNO ₃ , 80–90 °C	Labile sulfides and inclusions, including Fe _{1-x} S, ZnS, chalcopyrite (CuFeS ₂), and Cu-bearing sulfosalts
3. Cyanide Re-Leach	NaCN (post-acid step)	Metals associated with reactive sulfides such as pyrite (FeS ₂) and arsenian pyrite (FeAsS)
4. Aqua Regia Digestion	HCl + HNO ₃ (3:1)	Relatively inert sulfides and carbonate/silicate-associated metal fractions
5. Fire Assay	PbO-based flux fusion, \sim 1000 °C	Remaining unrecovered metal inventory hosted in refractory sulfide and silicate matrices

The diagnostic leaching procedure was applied exclusively to support qualitative and quantitative inference of metal deportment and accessibility, rather

than to derive kinetic parameters. Time-dependent dissolution behavior and rate-controlling mechanisms were evaluated independently through dedicated kinetic leaching experiments, as described in subsequent sections.

2.5 Cyanidation leaching experiments

Cyanidation leaching experiments were conducted in a baffled, open-tank laboratory reactor to promote hydrodynamically uniform mixing and minimize dead-zone stagnation during slurry conditioning. A 6.8 kg composite ore feed, previously homogenized to preserve size–density representativeness, was combined with 9.4 L of distilled water, producing a slurry at approximately 42 wt% solids.

The initial pulp pH (≈ 8.55) was adjusted and maintained within pH 10.0–10.3 using CaO addition to ensure alkaline conditions conducive to cyanide stability and to suppress volatilization of HCN(g). Sodium cyanide (NaCN) was used as the primary lixiviant and dosed to an initial concentration of 600 mg/L, thereby establishing reagent-sufficient conditions throughout the 54 h leaching period.

Dissolved oxygen (DO) was monitored continuously using a calibrated optical DO probe (Hanna HI9147). As the reactor operated under open-tank agitation without gas sparging or forced aeration, DO levels were not externally controlled and were allowed to evolve naturally through atmospheric oxygen exchange and ore-driven redox reactions.

To introduce a discrete and quantifiable oxygen impulse for short-duration surface oxidation, 3 mL of 30 wt% H₂O₂ was added at $t = 0$ h. This limited oxidant addition was intended to assist transient surface conditioning of labile sulfide phases that may form sulfur-rich or Fe-bearing surface films over precious-metal inclusions. Owing to laboratory constraints that precluded continuous oxidant dosing or oxygen sparging, H₂O₂ was applied only intermittently and functioned as a short-term oxygen supplement, rather than as a sustained pretreatment or kinetic variable.

Time-resolved slurry sampling was performed at $t = 0, 2, 4, 8, 24, 48,$ and 54 h to capture intrinsic metal dissolution behavior and reagent-consumption evolution. At each interval, approximately 65 mL of well-mixed slurry was withdrawn and immediately separated by centrifugation into solids and pregnant leach solution (PLS). A 20 mL aliquot of clarified PLS was retained for Flame AAS determination of Au, Ag, and Cu using identical calibration protocols to ensure analytical equivalence across all samples. Concurrently, pulp pH and DO were recorded.

Following aliquot retention, all solids and remaining solution were returned to the reactor, and 20 mL of distilled make-up water was added to maintain the slurry at approximately 42 wt% solids. This procedure preserved a consistent mass balance and solution chemistry framework for subsequent kinetic interpretation and inventory-based metal recovery calculations.

2.6 Reagent inventory-based metal recovery and cyanide consumption calculations

Gold (Au), silver (Ag), and copper (Cu) extraction, together with sodium cyanide consumption, were quantified using cumulative inventory-based mass balance approaches that explicitly account for solution sampling throughout the experiment.

The percentage extraction of metal i ($i = \text{Au, Ag, Cu}$) at leaching time t was calculated according to Eq. (1):

$$E_i(t) (\%) = \frac{M_{i,aq}(t) + \sum M_{i,removed}(t)}{M_{i,aq}(t_f) + M_{i,res}(t_f)} \times 100 \quad (1)$$

where $M_{i,aq}(t)$ is the aqueous metal inventory of metal i at time t (mg), $\sum M_{i,removed}(t)$ is the cumulative mass of metal i removed with solution samples up to time t (mg), t_f is the final leaching time (54 h), $M_{i,aq}(t_f)$ is the aqueous metal inventory at the end of leaching (mg), and $M_{i,res}(t_f)$ is the metal inventory remaining in the solid residue at the end of the test (mg); all inventories are reported on a consistent mass basis, yielding dimensionless extraction values expressed as percentages.

Sodium cyanide consumption per metric ton of dry ore at leaching time t was calculated using a free cyanide inventory balance, as given in Eq. (2):

$$NaCN_{cons}(t) = \frac{\sum NaCN_{added}(t) - NaCN_{free,aq}(t) - \sum NaCN_{removed}(t)}{W_{ore}} \quad (2)$$

where $NaCN_{cons}(t)$ is the sodium cyanide consumption (kg NaCN/t dry ore), $\sum NaCN_{added}(t)$ is the cumulative mass of sodium cyanide added up to time t (kg), $NaCN_{free,aq}(t)$ is the free cyanide inventory in the aqueous phase at time t (kg), $\sum NaCN_{removed}(t)$ is the cumulative mass of cyanide removed with solution samples up to time t (kg), and W_{ore} is the dry ore mass (t).

The free cyanide inventory in solution at time t was calculated from the measured free cyanide concentration and solution volume according to Eq. (3):

$$NaCN_{free,aq}(t) = C_{CN}(t)V(t) \quad (3)$$

where $C_{CN}(t)$ is the free cyanide concentration in solution (g/L) and $V(t)$ is the solution volume at time t (L).

2.7 Rate-controlling mechanism and kinetic model fitting

The rate-controlling mechanisms governing gold (Au) and silver (Ag) dissolution during cyanidation were evaluated using the Shrinking Core Model (SCM) as a conceptual framework for heterogeneous leaching kinetics. In the SCM description, an ore particle is idealized as a reacting sphere in which the reaction interface migrates inward as leaching proceeds, resulting in a progressively shrinking unreacted core.

Depending on physicochemical conditions and mineral texture, the overall dissolution rate may be governed by (i) diffusion through the external liquid film, (ii) surface chemical reaction at the particle–solution interface, or (iii) diffusion through reaction products accumulated at or near the particle surface.

Under the experimental conditions applied in this study, namely fine particle size, vigorous mechanical agitation, and reagent-sufficient alkaline cyanidation, the contribution of external liquid-film diffusion to the overall rate resistance is reasonably expected to be negligible. Numerous cyanidation studies have demonstrated that, for well-agitated slurries and finely ground feeds, liquid-film mass-transfer resistance is minor relative to intrinsic surface reaction and internal diffusion processes [23], [24]. Accordingly, external film-diffusion control was not considered an active rate-limiting mechanism in the present kinetic evaluation.

Kinetic interpretation therefore focused on two SCM-consistent rate-controlling regimes:

- (i) surface chemical reaction control, and
- (ii) diffusion through a product (ash) layer.

Previous investigations of gold cyanidation kinetics in sulfide-bearing systems have shown that dissolution behavior may exhibit mixed or evolving control between these two regimes due to diffusional resistance and surface passivation effects, without restriction to a specific genetic ore type [23], [24]. In the present work, these general kinetic concepts are interpreted in the specific context of the Mount Muro low-sulfidation epithermal (LSE) ore system, informed by experimental observations and the mineralogical characteristics of the feed.

2.7.1 SCM linearization for rate-controlling mechanism diagnosis

To diagnose the apparent rate-controlling regime and evaluate potential temporal evolution in dissolution behavior, time-resolved cyanidation data were transformed using classical linearized SCM expressions for spherical particles corresponding to surface chemical reaction control and product-layer diffusion control [25].

Surface chemical reaction control is expressed as Eq. (4):

$$1 - (1 - X_t)^{\frac{1}{3}} = kt \quad (4)$$

Product (ash) layer diffusion control is expressed as Eq. (5):

$$1 - 3(1 - X_t)^{\frac{2}{3}} + 2(1 - X_t) = kt \quad (5)$$

where X_t is the dimensionless fraction of Au or Ag transferred into solution at leaching time t , and k is the apparent rate constant (h^{-1}).

SCM linearization was applied using a multi-window regression strategy to assess both overall and time-dependent kinetic behavior:

1. Global regression incorporating all sampling times (2, 4, 8, 24, 48, and 54 h);
2. Early-time window representing the initial dissolution stage (2, 4, and 8 h);
3. Extended-time window capturing later-stage dissolution behavior (8, 24, 48, and 54 h).

Linear conformity between experimental data and each SCM transformation was assessed using the coefficient of determination (R^2). Importantly, SCM linearization was applied exclusively as a mechanistic diagnostic tool, rather than as a predictive kinetic model, providing a structured basis for interpreting time-dependent dissolution behavior.

2.7.2 SCM-Integrated kinetic model fitting

Beyond SCM linearization, a suite of kinetic models that integrate or are conceptually consistent with the shrinking-core framework was applied to the same time-resolved cyanidation dataset. The objective of this analysis was to evaluate overall kinetic conformity and parameter plausibility across different theoretical formulations, rather than to perform purely empirical curve fitting.

The models considered include the Mintek, KBK, Crundwell, Ling, and Loveday models, which collectively span empirical, semi-mechanistic, and mechanistic representations of gold cyanidation kinetics (Table 2). All governing equations follow their original literature definitions and are summarized in Table 3; no modification or re-derivation of published formulations was introduced.

In this study, kinetic modeling is applied as an interpretive framework to elucidate time-dependent dissolution behavior in a sulfide-bearing LSE gold system. Specifically, the modeling approach is used to:

- Identify dominant rate-controlling mechanisms,
- Assess the influence of diffusional resistance and surface passivation, and
- Provide mechanism-based guidance for subsequent geometallurgical interpretation.

All SCM-integrated kinetic models were fitted using a single global regression domain covering all sampling times (2–54 h) for Au and Ag independently. Temporal evolution in rate control was evaluated separately through SCM linearization; consequently, no time segmentation was applied during kinetic model fitting.

2.8 Statistical correlation analysis

Statistical correlation analysis was applied independently of kinetic modeling to evaluate intrinsic inter-metal associations and their mineralogical implications. Pearson correlation coefficients (r) were calculated to assess linear relationships among Au, Ag, and Cu grades, as well as particle-size distribution parameters, in both feed material and cyanidation residues.

Table 2. Equation of kinetic models integrating the shrinking core concept

Model	Formula
Mintek model [26]	$-r_{Au} = k([Au]_p - [Au]_{p,\infty})^2$
KBK model [25]	$[Au]_p(t) = [Au]_{p,\infty} + [(Au]_{p,0} - [Au]_{p,\infty})^{(1-n)} + (n-1)kt]^{(1/(1-n))}$
Crundwell model [23]	$\frac{dX}{dt} = k_s(1-X)^{\frac{2}{3}}(1-f)$ $k_s = \frac{3(k_a k_c [CN^-][O_2])^{0.5}}{\rho_{Au}}$ $\frac{df}{dt} = k_2(1-f) - k_{-2}f + \frac{2}{3}k_s f(1-f)(1-X)^{-\frac{1}{3}}$
Ling model [24]	$-\frac{d[Au]_p}{dt} = k'[CN^-]^a [O_2]^b ([Au]_p - [Au]_{p,\infty})^c$
Loveday model	$[Au]_p(t) = ([Au]_{p,0} - [Au]_{p,\infty}) \left(1 + \frac{n}{n+1} k_{max} t\right) + [Au]_{p,0}, t \leq \frac{1}{k_{max}}$ $[Au]_p(t) = \frac{[Au]_{p,0} - [Au]_{p,\infty}}{n+1} \left(\frac{1}{k_{max} t}\right)^n + [Au]_{p,0}, t \geq \frac{1}{k_{max}}$

*Notes:

- r_{Au} — rate of gold dissolution ($\text{mol}\cdot\text{m}^{-2}\cdot\text{s}^{-1}$)
- $[CN^-]$ — cyanide ion concentration ($\text{mol}\cdot\text{L}^{-1}$)
- $[O_2]$ — dissolved oxygen concentration ($\text{mol}\cdot\text{L}^{-1}$)
- k_{CN}, k_{O_2} — mass transfer coefficients for cyanide and oxygen diffusion through the liquid film ($\text{m}\cdot\text{s}^{-1}$)
- k — apparent rate constant (h^{-1})
- $[Au]_p$ — instantaneous gold concentration in solution at time t ($\text{mg}\cdot\text{L}^{-1}$ or $\text{g}\cdot\text{t}^{-1}$)
- $[Au]_{p,\infty}$ — equilibrium gold concentration after infinite leaching time ($\text{mg}\cdot\text{L}^{-1}$ or $\text{g}\cdot\text{t}^{-1}$)
- n — Schumann distribution parameter for reaction sites
- k_{max} — maximum leaching rate constant (h^{-1})
- t — leaching time (h)
- k' — overall rate constant (empirical)
- a, b, c — reaction orders with respect to cyanide, oxygen, and unreacted gold concentration
- X — fractional conversion of the leaching reaction
- f — fraction of particle surface covered by a passive film
- k_s — overall surface rate constant ($\text{m}\cdot\text{s}^{-1}$)
- k_a, k_c — anodic and cathodic reaction rate constants
- k_2, k_{-2} — rate constants for film formation and dissolution
- ρ_{Au} — density of gold ($\text{g}\cdot\text{cm}^{-3}$)

Strong positive correlations ($r \geq 0.85$) were interpreted as indicative of shared mineralogical hosts or phase coexistence, whereas weak to moderate correlations were considered reflective of minor or indirect associations. Correlation matrices were constructed separately for feed and residue samples to identify changes in metal associations induced by

leaching. Statistical significance was evaluated at the 95% confidence level ($p < 0.05$).

3 Results and discussion

3.1 Ore feed characteristics and gold deportment

3.1.1 Ore feed characteristics and gold deportment

The Mount Muro ore feed is derived from a low-sulfidation epithermal (LSE) gold system characterized by silica-dominated gangue mineralogy and structurally controlled quartz-carbonate veining. Secondary mineralogical data compiled from Syaban et al. (2024) [9] indicate that mineralization is associated with well-developed silicification, argillic, propylitic, and sericitic alteration assemblages. Together, these alteration styles define the mineralogical framework governing precious-metal deportment and are consistent with hydrothermal conditions typical of LSE systems formed from reduced to near-neutral fluids.

Gold occurs predominantly as electrum (Au–Ag alloy), with subordinate native gold, whereas silver is present both as a constituent of electrum and as discrete silver sulfides and argentian sulfosalts. Copper is hosted mainly in chalcopyrite, bornite, and tetrahedrite-tennantite group minerals, reflecting the polymetallic character commonly observed in LSE deposits [9]. Petrographic observations reported in prior studies indicate that precious metals are typically present as fine inclusions, solid solutions, replacement textures, or disseminated grains within sulfide and sulfosalt matrices, with only a limited proportion occurring as visibly coarse native-metal particles.

In the present study, mineralogical deportment is described strictly in terms of host-mineral association and textural occurrence. The term free-milling, used subsequently, is defined operationally based on diagnostic leaching response rather than petrographic liberation alone. This distinction is essential to avoid overinterpretation of metallurgical behavior based solely on textural observations and establishes a consistent geometallurgical baseline for interpreting size-dependent metal distribution and leaching response in the following sections.

3.1.2 Particle size distribution and size-dependent metal distribution

The prepared ore feed exhibits a fine particle size distribution with a P_{80} of approximately $54 \mu\text{m}$, which is finer than that typically applied in conventional cyanidation practice ($P_{80} \approx 75 \mu\text{m}$). This grind size was deliberately selected to ensure representative exposure of precious-metal-bearing phases characteristic of LSE systems—particularly electrum and native Au–Ag alloys—while maintaining realistic particle-scale conditions for subsequent cyanidation leaching and kinetic evaluation. In deposits such as Mount Muro,

precious metals commonly occur as fine inclusions or replacement textures within sulfide and sulfosalt assemblages, necessitating relatively fine grinding to enhance effective surface accessibility.

Triplicate head-grade assays of the homogenized feed (Table 3) yielded average grades of 1.45 g/t Au, 2.47 g/t Ag, and 32.5 g/t Cu, with low relative standard deviations (2.1–2.3%) and narrow 95% confidence intervals (± 4.1 – 4.6%). These results confirm a high degree of feed homogeneity and analytical reliability, providing a robust basis for evaluating size-dependent metal distribution without bias arising from sampling variability.

Table 3. Triplicate head-grade assays of the ore feed

Sample	Au (g/t)	Ag (g/t)	Cu (g/t)
Replicate 1	1.48	2.40	32
Replicate 2	1.46	2.50	33
Replicate 3	1.42	2.50	33
Average	1.45	2.47	32.5

Table 4. Size-by-size distribution of gold, silver, and copper in the ground ore feed

Size (μm)	Mass (%)	Contents (g/t)			Metal Distribution (%)		
		Au	Ag	Cu	Au	Ag	Cu
+150	2.55	0.85	1.4	38	1.5	1.3	3.0
-150 +75	8.87	0.96	1.7	27	6.0	5.6	7.4
-75 +38	18.34	0.95	1.5	24	12.2	10.2	13.6
-38	70.23	1.63	3.2	35	80.3	83.0	76.0
Total	100	1.43	2.7	32	100	100	100

Size-by-size analysis of the ground feed (Table 4) demonstrates a pronounced concentration of metals in the finest particle fractions. The $-38 \mu\text{m}$ size class, which accounts for 70.23% of the total mass, hosts the majority of the contained metals, comprising approximately 80.3% of total Au, 83.0% of Ag, and 76.0% of Cu. Correspondingly, gold and silver grades increase systematically with decreasing particle size, with Au grades rising from approximately 0.85 g/t in the $+150 \mu\text{m}$ fraction to 1.63 g/t in the $-38 \mu\text{m}$ fraction, and Ag grades increasing from approximately 1.4 to 3.2 g/t over the same size range.

In contrast, copper grades exhibit relatively limited variation across size fractions, indicating a more uniform grade distribution compared with Au and Ag. Nevertheless, owing to the mass dominance of the finest fraction, copper deportment remains strongly concentrated in the $-38 \mu\text{m}$ size class. This behavior is consistent with copper being hosted primarily in fine-grained sulfide and Cu–Ag sulfosalt minerals typical of LSE mineralization, rather than exhibiting strong size-selective enrichment.

Overall, the preferential enrichment of Au and Ag in the finest size fraction reflects the combined effects of mineralogical association and comminution response characteristic of low-sulfidation epithermal ores, in which precious metals are commonly hosted as fine inclusions or replacement textures within sulfide and

sulfosalt matrices. As documented for Mount Muro by Syaban et al. (2024) [9], these size-dependent distribution characteristics provide the quantitative foundation for the correlation-based mineralogical interpretation presented in Section 3.1.3 and for the accessibility domains evaluated through diagnostic leaching in Section 3.1.4.

3.1.3 Metal correlation and mineralogical implications

Pearson correlation analysis was applied to the size-fractionated ore feed to evaluate intrinsic metal associations and their mineralogical significance within a low-sulfidation epithermal (LSE) framework. This analysis provides a quantitative complement to the size-distribution results presented in Section 3.1.2 by assessing whether metals exhibit shared or independent deportment at the particle scale. The resulting correlation coefficients and their geometallurgical interpretations are summarized in Table 5.

A very strong positive correlation between Au and Ag ($r = 0.996$) indicates that these metals are predominantly co-hosted within the same mineralogical domains. This relationship is most plausibly attributed to electrum and native Au–Ag alloys, which constitute the principal precious-metal carriers in the Mount Muro LSE system. This interpretation is fully consistent with mineralogical descriptions reported by Syaban et al. (2024) [9], which identify electrum as the dominant Au–Ag phase, accompanied by subordinate Ag-bearing sulfides and Cu–Ag sulfosalts.

In contrast, weak correlations are observed between Au–Cu ($r = 0.28$) and Ag–Cu ($r = 0.32$), indicating that copper-bearing minerals do not act as primary hosts for precious metals in the ore feed. Copper is therefore inferred to reside predominantly in discrete sulfide and sulfosalt phases, including chalcopyrite, subordinate bornite, and tetrahedrite–tennantite, which are mineralogically and chemically distinct from the dominant electrum-hosted Au–Ag assemblage at this stage. The limited Au–Cu and Ag–Cu associations suggest that any spatial proximity between precious metals and Cu-bearing phases is minor and does not reflect systematic structural incorporation.

Strong correlations between gold grade and particle-size parameters further demonstrate pronounced size-dependent enrichment of Au. The positive correlation with mass percentage and the strong negative correlation with cumulative passing fraction indicate preferential concentration of gold in the finest size classes. This behavior is consistent with LSE-typical textural characteristics, in which precious metals commonly occur as fine inclusions, replacement features, or disseminated grains within sulfide–sulfosalt matrices, rather than as coarse, discrete native particles. These textural controls align with the fine-fraction enrichment observed in Section 3.1.2 and reinforce the interpretation that particle size and mineralogical hosting jointly govern gold distribution in the feed.

Overall, the correlation patterns define a coherent mineralogical framework in which Au and Ag are

tightly coupled and preferentially concentrated in fine particle-size fractions, while Cu exhibits largely independent deportment. This framework provides a robust geometallurgical basis for interpreting the size-dependent metal distribution discussed in Section 3.1.2 and for contextualizing the accessibility domains subsequently identified through diagnostic leaching in Section 3.1.4. Together, these observations establish a consistent foundation for interpreting the contrasting extraction behavior of Au and Ag examined in Section 3.2.

Table 5. Pearson correlation coefficients and inferred mineralogical implications for the Mount Muro ore feed

Relationship	Correlation (r)	Mineralogical implication (LSE-consistent)
Au–Ag	0.996	Strong statistical co-occurrence, indicating electrum and native Au–Ag alloys as the dominant precious-metal hosts, with subordinate Ag hosted in sulfides and Cu–Ag sulfosalts
Au–Cu	0.28	Weak association, suggesting limited linkage between Au and Cu-bearing sulfides (e.g., chalcopyrite ± bornite)
Ag–Cu	0.32	Minor association, consistent with limited occurrence of argentine Cu–Ag sulfosalts (e.g., tetrahedrite–tennantite)
Au–Mass %	0.99	Preferential enrichment of Au in fine particle-size fractions
Au–Cum. Pass %	–0.98	Progressive decrease in Au content with increasing particle size

Overall, the correlation patterns define a coherent mineralogical framework in which Au and Ag are tightly coupled and preferentially concentrated in fine particle-size fractions, while Cu exhibits largely independent deportment. This framework provides a robust geometallurgical basis for interpreting the size-dependent metal distribution discussed in Section 3.1.2 and for contextualizing the accessibility domains subsequently identified through diagnostic leaching in Section 3.1.4. Together, these observations establish a consistent foundation for interpreting the contrasting extraction behavior of Au and Ag examined in Section 3.2.

3.1.4 Diagnostic leach interpretation

Diagnostic leaching quantifies the relative accessibility of gold (Au) and silver (Ag) across operationally defined accessibility domains, based on their response to sequential chemical treatments. These domains reflect differences in cyanide amenability under standardized conditions and are not intended to correspond directly to discrete mineralogical phases.

Accordingly, diagnostic leaching provides an independent geometallurgical perspective that complements the mineralogical framework established for the Mount Muro low-sulphidation epithermal (LSE) system [9].

At the diagnostic grind size ($P_{80} \approx 75 \mu\text{m}$), gold exhibits high cyanide accessibility, with 79.9% classified as free-milling as shown in Table 6. The comparatively minor proportions of gold associated with sulfide-related domains (13.1% cumulatively) and the limited silicate-locked fraction (3.5%) indicate that quartz encapsulation is not the primary source of metallurgical resistance for gold in this ore. Instead, the majority of Au-bearing phases—predominantly electrum and native gold typical of LSE mineralization—are effectively exposed under the applied comminution conditions. These results are consistent with the strong Au–Ag association and fine-fraction enrichment identified in Sections 3.1.2 and 3.1.3.

Table 6. Diagnostic leach-based accessibility domains and mineralogical interpretation of gold and silver

Diagnostic Accessibility Domain	Gold (%)	Silver (%)	Dominant Host Minerals (Mount Muro LSE)	Chemical Formulae
Free-milling (cyanide-amenable)	79.9	53.9	Electrum, native gold, native silver	Au–Ag (electrum), Au ⁰ , Ag ⁰
Labile sulfides	6.5	5.9	Galena, sphalerite (minor inclusion hosts)	PbS, ZnS
Active sulfides	6.6	17.7	Pyrite, chalcopyrite ± bornite	FeS ₂ , CuFeS ₂ , Cu ₅ FeS ₄
Inert sulfides + carbonates	3.5	21.7	Acanthite–argentite, tetrahedrite–tennantite, carbonate gangue	Ag ₂ S, (Cu,Fe) ₁₂ S ₄ As ₄ S ₁₃ , (Cu,Fe) ₁₂ As ₄ S ₁₃ , CaCO ₃
Refractory (silicate-locked)	3.5	0.7	Quartz-hosted inclusions, clay-associated domains (illite–smectite)	SiO ₂ , illite–smectite
Total	100	100	—	—

* Note: Accessibility domains are operationally defined based on sequential leaching response and may reflect limitations in chemical reactivity and effective surface accessibility in addition to mineralogical association.

Silver displays a more complex diagnostic deportment. Only 53.9% of Ag reports to the free-milling fraction, while substantial proportions are associated with active sulfide (17.7%) and inert sulfide–carbonate (21.7%) domains. This distribution reflects

the dual occurrence of silver in LSE systems, where Ag is present both as a constituent of electrum and as discrete Ag sulfides (acanthite–argentite) and Cu–Ag sulfosalts (tetrahedrite–tennantite), consistent with the documented mineralogy of Mount Muro [9]. Importantly, these domains may include silver that is texturally exposed yet exhibits a delayed chemical response, owing to differences in cyanide complex stability and intrinsic dissolution kinetics between $\text{Ag}(\text{CN})_2^-$ and $\text{Au}(\text{CN})_2^-$ under alkaline conditions.

It is therefore emphasized that diagnostic leaching captures an operational response to cyanide chemistry rather than a direct quantitative partitioning of mineralogical phases. Differences in Au and Ag deportment observed in diagnostic leaching do not imply fundamentally different mineral systems; instead, they reflect asymmetries in chemical reactivity and effective surface accessibility inherent to low-sulphidation epithermal mineralization.

Overall, the diagnostic leach results establish a static geometallurgical baseline by delineating the relative cyanide amenability of Au- and Ag-bearing domains under standardized conditions. This baseline provides essential context for interpreting the time-resolved extraction behavior of Au and Ag during continuous cyanidation (Section 3.2) and for evaluating the residual mineralogical controls examined through residue characterization and size-dependent recovery analysis in Section 3.3.

3.2 Gold and silver extraction behavior and reagent consumption

Gold and silver exhibit distinctly different time-dependent extraction behaviors during alkaline cyanidation, despite their close mineralogical association within the Mount Muro low-sulphidation epithermal (LSE) system. This divergence does not reflect fundamentally different mineral systems, but instead arises from intrinsic asymmetry in cyanide complex chemistry coupled with differences in effective surface accessibility from the onset of leaching.

Under alkaline conditions, gold forms the highly stable and readily soluble $\text{Au}(\text{CN})_2^-$ complex, whereas silver forms $\text{Ag}(\text{CN})_2^-$ with lower thermodynamic stability and slower intrinsic dissolution kinetics. Consequently, gold dissolution systematically precedes silver, even when both metals coexist within the same electrum grains, as widely documented in cyanidation studies [2]. From a mineralogical perspective consistent with Syaban et al. (2024) [9], gold at Mount Muro occurs predominantly as electrum and native Au–Ag alloys that are highly reactive toward cyanide. Silver, in contrast, is partitioned between electrum and more chemically resistant hosts, including silver sulfides (acanthite–argentite) and Cu–Ag sulfosalts (e.g., tetrahedrite–tennantite), which exhibit reduced reactivity during cyanidation. The combined effect of these chemical and mineralogical contrasts is reflected directly in the time-resolved extraction profiles shown in Figure 1.

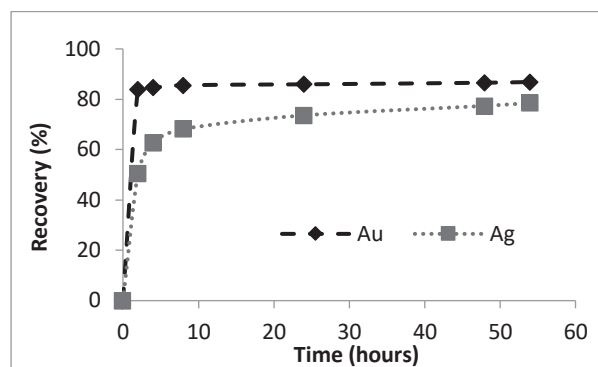


Fig. 1. Gold and silver extraction profiles during cyanidation under the following conditions: 42% solid slurry concentration, 600 Mg/L NaCN, pH 10.2, and hydrogen peroxide (H_2O_2) addition over a leaching period of 54 hours.

Experimentally, gold extraction increased rapidly, reaching 83.9% within the first 2 h of leaching, followed by only a marginal increase to 86.9% after 54 h (Figure 1). This pronounced early-stage extraction coincides with the period of highest reagent activity.

During this interval, cyanide consumption reached approximately 0.48 kg/t, while cumulative hydrogen peroxide consumption reached approximately 0.43 kg/t (Figures 2 and 3). Dissolved oxygen (DO) increased sharply from an initial slurry value of ~0.3 ppm to 13–14 ppm following H_2O_2 addition (Figure 2), and free cyanide concentration was maintained through intermittent dosing (Figure 3). Once readily accessible electrum and native Au–Ag surfaces were largely depleted, the rate of further gold extraction declined markedly, despite sustained cyanide availability and relatively stable DO conditions throughout the remainder of the leaching period. This behavior indicates that gold dissolution becomes progressively constrained by declining effective surface accessibility rather than by reagent limitation.

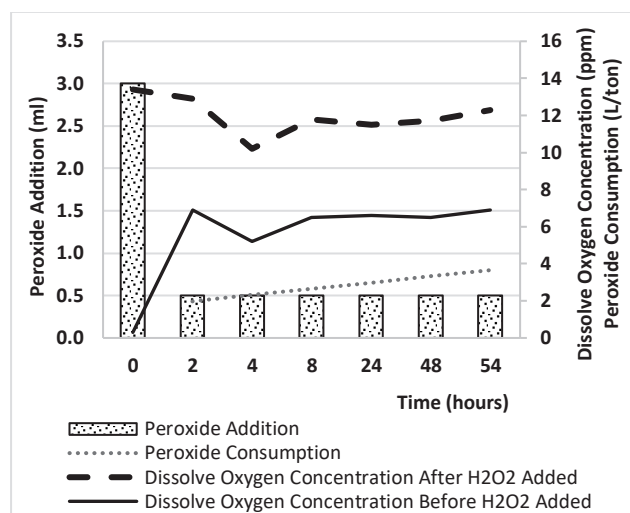


Fig. 2. Hydrogen peroxide addition, dissolved oxygen concentration in the slurry, and cumulative peroxide consumption during the leaching process.

In contrast, silver extraction progressed more gradually, increasing from 50.5% at 2 h to 78.5% after 54 h (Figure 1). This delayed extraction trajectory was accompanied by a monotonic increase in cyanide

consumption to approximately 1.63 kg/t, under comparatively stable DO conditions (~5–7 ppm prior to peroxide addition and ~10–12 ppm thereafter; Figures 2 and 3). The slower and more sustained extraction response of silver is consistent with its dual department in LSE systems: one fraction dissolves concurrently with gold from electrum, whereas a substantial proportion remains associated with more resistant Ag sulfides and Cu–Ag sulfosalts, locally accompanied by Cu-bearing sulfides such as chalcopyrite ± bornite and pyrite, as reported for Mount Muro [9]. These phases impose persistent chemical and transport-related constraints on silver dissolution, even under reagent-sufficient conditions.

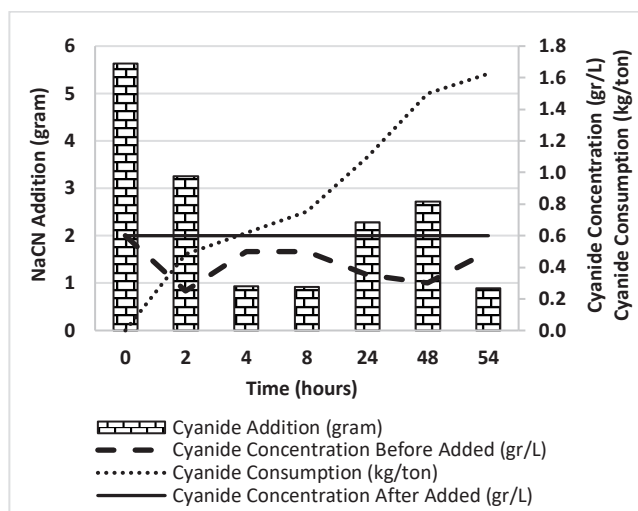


Fig. 3. Cyanide addition, cyanide concentration in slurry, and cumulative cyanide consumption during the leaching process.

Importantly, the persistence of unrecovered Au and Ag after extended leaching cannot be attributed to insufficient leaching time or inadequate reagent supply. Instead, it reflects residual mineralogical domains and surface-related accessibility constraints that progressively limit effective metal dissolution once the most reactive surfaces are exhausted. These constraints are examined directly through post-leaching residue characterization and size-by-size metal recovery analysis in Section 3.3, which provides the mineralogical and physical basis for the kinetic interpretations developed in the subsequent sections.

3.3 Residue characterization and metal recovery by size fraction

Characterization of cyanidation residues provides direct physical and mineralogical evidence for the persistence of unrecovered metals following leaching, particularly in low-sulphidation epithermal (LSE) systems such as Mount Muro. Whereas time-resolved extraction data describe the overall metallurgical response (Section 3.2), residue analysis elucidates why complete metal recovery is not achieved under reagent-sufficient conditions. In LSE deposits, precious metals are dominantly hosted in electrum and native Au–Ag alloys, with additional contributions from Ag sulfides and Cu–Ag sulfosalts, which exert first-order control on residual

metal behavior during cyanidation. By integrating residue particle-size distribution, residual metal grades, inventory partitioning, correlation analysis, and size-by-size recovery, this section establishes a direct and internally consistent link between comminution response, leaching performance, and the kinetic interpretations developed subsequently.

3.3.1 Metal distribution by particle size in cyanidation residue

Post-leaching sieve analysis demonstrates that the cyanidation residue is strongly dominated by fine particles. As summarized in Table 7, the –38 μm fraction accounts for 65.35% of the total residue mass and hosts the majority of the residual metal inventory, comprising 65.19% of residual Au, 69.35% of residual Ag, and 68.67% of residual Cu. This distribution reflects not only the mass dominance of fine particles, but also the limited reactive accessibility of mineral phases typical of LSE systems once the most readily leachable surfaces have been exhausted.

Excluding the coarsest fraction (+150 μm), residual gold grades across the –150 +75, –75 +38, and –38 μm fractions are essentially uniform, ranging narrowly between ~0.19 and 0.20 g/t. This near-constancy indicates that unrecovered gold is not progressively enriched with decreasing particle size, but instead persists at similar concentrations once the more accessible coarse material, commonly associated with exposed electrum or native gold, has been preferentially dissolved during the early stages of cyanidation. Silver exhibits a comparable pattern, with relatively uniform grades across the fine fractions and only minor enrichment in the –38 μm fraction, consistent with its mixed department between electrum and Ag-sulfide phases such as acanthite–argentite.

Copper displays a tendency toward higher grades in the coarser fractions; however, owing to the overwhelming mass contribution of the –38 μm fraction, the overall residual Cu inventory remains dominated by fine particles. This behavior reflects the persistence of Cu-bearing sulfides and Cu–Ag sulfosalts, which are characteristically fine-grained and exhibit low reactivity under alkaline cyanidation conditions.

Table 7. Sieve analysis and metal grades in leach residue

Size (μm)	Mass (%)	Contents (g/tonne)			Metal Distribution (%)		
		Au	Ag	Cu	Au	Ag	Cu
+150	2.62	0.3	1.2	32	3.92	4.76	3.52
-150 +75	10.63	0.2	0.6	24	10.6	9.67	10.72
-75 +38	21.4	0.19	0.5	19	20.29	16.22	17.09
-38	65.35	0.2	0.7	25	65.19	69.35	68.67
Total	100	0.2	0.66	24	100	100	100

The concentration of residual Au and Ag within the –38 μm fraction demonstrates that metal persistence is not controlled by insufficient grinding or coarse-particle

shielding. Instead, residual precious metals are governed by accessibility constraints imposed by mineralogical hosting and surface-related factors characteristic of LSE mineralization. These include partial encapsulation of electrum within sulfide matrices, association with Ag sulfides and Cu–Ag sulfosalts (e.g., tetrahedrite–tennantite), sub-micron inclusions, and reduced surface reactivity under cyanidation conditions. These observations are fully consistent with the diagnostic leaching results presented in Section 3.1.4, which identified sulfide- and sulfosalt-associated domains as the dominant contributors to residual metal persistence.

3.3.2 Metal correlations and mineralogical implications in residue

Correlation analysis provides further insight into the mineralogical controls governing residual metal distribution following cyanidation, complementing the size-based residue characteristics discussed in Section 3.3.1. As summarized in Table 8, the extremely strong Au–Ag correlation observed in the feed ($r = 0.996$), which reflects dominant electrum-hosted mineralization, remains high in the cyanidation residue ($r = 0.98$). This persistence indicates incomplete dissolution of electrum and native Ag-bearing phases despite prolonged leaching under reagent-sufficient conditions, confirming that a fraction of these phases remains effectively inaccessible rather than chemically non-reactive.

In contrast, correlations involving copper increase markedly after leaching. The Au–Cu correlation increases from 0.28 in the feed to 0.91 in the residue, while the Ag–Cu correlation increases from 0.32 to 0.96. This systematic strengthening indicates preferential co-retention of Au, Ag, and Cu within refractory Cu-bearing sulfides and Cu–Ag sulfosalts that persist through cyanidation. In the Mount Muro low-sulphidation epithermal (LSE) system, these phases are interpreted to include chalcopyrite, pyrite, and Cu–Ag sulfosalts of the tetrahedrite–tennantite series, together with Ag sulfides such as acanthite–argentite.

Importantly, the similarity of Au–Cu and Ag–Cu correlations in the feed (both weak and comparable in magnitude) demonstrates that neither gold nor silver is structurally hosted by copper minerals prior to leaching. The strong Au–Cu and Ag–Cu correlations observed in the residue therefore do not reflect primary mineralogical association, but rather selective depletion of more accessible Au–Ag phases during cyanidation, leaving behind residual precious metals that are spatially associated with refractory Cu-bearing assemblages. This distinction is critical: the post-leaching Au–Cu association arises from co-retention, not from co-deposition.

Correlations between gold and particle-size metrics also evolve systematically as a consequence of selective dissolution. In the feed, gold exhibits strong positive correlation with fine-fraction mass and strong negative correlation with cumulative passing percentage, reflecting preferential enrichment of Au in fine epithermal vein and breccia domains. In the residue, these relationships reverse, indicating that the most

accessible gold, irrespective of particle size, has been preferentially removed, and that residual gold is dominated by fine-grained, low-reactivity domains associated with sulfide and sulfosalt matrices. This reversal confirms that residual metal persistence is governed by mineralogical accessibility and surface reactivity rather than by incomplete liberation or inadequate comminution.

Table 8. Comparison of metal correlations and mineralogical implications between feed and leach tailing (LS epithermal-consistent)

Relationship	Feed		Tailing	
	Correlation (r)	Mineralogical Implication	Correlation (r)	Mineralogical Implication
Au–Ag	0.996	Dominant co-occurrence as electrum and native Au–Ag alloys typical of low-sulphidation epithermal veins	0.98	Partial persistence of electrum and native Ag-bearing phases due to incomplete accessibility rather than chemical infeasibility
Au–Cu	0.28	Weak primary association, indicating Au is not structurally hosted by Cu-bearing sulfides	0.91	Strong co-retention of residual Au with refractory Cu-bearing sulfides and Cu–Ag sulfosalts following preferential dissolution of accessible Au
Ag–Cu	0.32	Minor association, consistent with limited presence of argentian Cu–Ag sulfosalts in the feed	0.96	Enhanced Ag–Cu association reflecting structural hosting of Ag in Cu–Ag sulfosalts and Ag sulfides (e.g., acanthite–argentite) resistant to cyanidation
Au–Mass %	0.99	Preferential enrichment of Au in fine epithermal vein and breccia domains	–0.51	Residual Au dominated by fine-grained, low-reactivity sulfide–sulfosalt-associated domains
Au–Cum. Pass %	–0.98	Systematic decrease in Au content with increasing particle size	0.51	Reversal due to preferential dissolution of accessible Au irrespective of particle size

Taken together, the correlation patterns demonstrate a progressive shift in metallurgical control during cyanidation. The feed is dominated by electrum-controlled Au–Ag associations characteristic of LSE mineralization, whereas the residue is increasingly governed by refractory sulfide- and sulfosalt-hosted domains in which Au and Ag are retained alongside Cu. This evolution provides a mineralogical explanation for the fine-fraction dominance observed in Section 3.3.1 and establishes a direct mechanistic bridge to the kinetic interpretations developed in Section 3.4, where diffusion- and accessibility-controlled dissolution behavior is shown to dominate the later stages of leaching.

3.3.3 Size-dependent metal recovery and residual accessibility

Size-by-size metal recovery calculations provide a quantitative framework for evaluating how mineralogical accessibility, rather than particle size alone, governs the differential leaching behavior of Au, Ag, and Cu during cyanidation summarized in Table 9. Gold recovery increases progressively with decreasing particle size, rising from 64.7% in the +150 μm fraction to 87.7% in the –38 μm fraction. This trend confirms that finer grinding enhances the initial exposure and accessibility of gold-bearing domains, particularly electrum and native Au–Ag alloys. However, when these recovery values are considered alongside the near-uniform residual Au grades observed across the fine fractions (Section 3.3.1), it becomes evident that recovery gains diminish once readily accessible gold surfaces are depleted. Beyond this point, further particle size reduction does not yield proportional improvements in gold recovery, indicating a transition from liberation-controlled to accessibility-controlled dissolution behavior. Residual gold persistence is therefore governed by mineralogical hosting, partial surface passivation, and micro-scale diffusional barriers rather than by incomplete comminution.

Table 9. Percentage of extraction of Au, Ag, and Cu for each size fraction

Size (μm)	% Recovery		
	Au	Ag	Cu
+150	64.7	14.3	15.8
-150 +75	79.2	64.7	11.1
-75 +38	80.0	66.7	20.8
-38	87.7	78.1	28.6

Silver recovery exhibits a stronger apparent dependence on particle size, increasing sharply from 14.3% in the +150 μm fraction to 78.1% in the –38 μm fraction. Despite this pronounced size effect, silver recovery remains consistently lower than gold across all size classes. This behavior reflects the more complex effective deportment of silver, wherein only a portion dissolves readily from electrum, while a substantial fraction remains hosted within Ag sulfides and Cu–Ag sulfosalts that respond slowly to cyanidation. Consequently, even at fine particle sizes where physical liberation is largely maximized, silver extraction

remains constrained by chemical reactivity and internal accessibility rather than by particle size alone.

Copper recovery remains uniformly low across all size fractions ($\leq 30\%$), demonstrating that Cu-bearing phases persist largely intact in the cyanidation residue. This behavior confirms that copper does not contribute materially to precious-metal dissolution under the applied conditions and instead serves as a tracer for refractory sulfide and sulfosalt domains that increasingly dominate residual metal associations following leaching.

Taken together, the size-dependent recovery trends summarized in Table 9 and interpreted mechanistically in Table 10 establish a clear hierarchy of controlling factors: gold exhibits a transition from liberation-controlled to accessibility-controlled dissolution, silver is constrained by diffusion- and reactivity-limited mechanisms even at fine sizes, and copper remains metallurgically inert under cyanidation conditions. These findings provide direct physical and mineralogical support for the kinetic interpretations developed in Section 3.4, where progressive loss of effective reactive surface area and increasing internal transport resistance are shown to govern Au and Ag dissolution behavior under reagent-sufficient conditions.

3.3.4 Synthesis and Implications

Residue-based size fractionation demonstrates that fine particles dominate both the mass of the cyanidation residue and the inventory of unrecovered metals. However, continued grinding beyond the applied P_{80} does not yield proportional recovery gains. The persistence of Au and Ag within the –38 μm fraction indicates that incomplete recovery is not governed by coarse-particle shielding or insufficient comminution.

Instead, residual metal losses are controlled by mineralogical accessibility constraints intrinsic to low-sulphidation epithermal systems. These constraints include hosting within sulfide and Cu–Ag sulfosalt phases, partial encapsulation of electrum, surface passivation during leaching, and micro-scale diffusional limitations. Once readily accessible electrum and native-metal surfaces are depleted, further dissolution becomes progressively constrained by the loss of effective reactive surface area rather than by particle size.

This synthesis establishes a clear physical and mineralogical basis for the kinetic behavior observed during cyanidation. The dominance of fine, low-reactivity residue domains directly supports the interpretation that gold dissolution transitions from initially rapid, surface-controlled behavior to mixed or diffusion-influenced kinetics, while silver dissolution remains diffusion-dominated throughout leaching. These observations provide the necessary foundation for the SCM-based mechanistic diagnosis and kinetic model discrimination developed in Section 3.4.

3.4 Identification of rate-controlling mechanisms

3.4.1 SCM-based mechanistic diagnosis of gold and silver dissolution

The rate-controlling mechanisms governing gold (Au) and silver (Ag) dissolution during cyanidation were evaluated using Shrinking Core Model (SCM) linearization applied over multiple time windows. This analysis establishes a mechanistic link between mineralogical accessibility (Sections 3.1–3.3), time-resolved extraction behavior (Section 3.2), and the kinetic model interpretation developed subsequently. The SCM framework is employed strictly as a diagnostic tool to assess whether dissolution behavior is more consistent with surface chemical reaction control, internal diffusion through a product layer, or mixed control, under reagent-sufficient and well-mixed conditions.

Table 10. Summary of SCM linearization parameters for gold and silver dissolution

Metal	Time window	SCM mechanism	k (h ⁻¹)	C	R ²
Au	Global (2–54 h)	Surface reaction	0.0006	0.4630	0.8396
		Product-layer diffusion	0.0008	0.4446	0.8403
	Early (2–8 h)	Surface reaction	0.0032	0.4502	0.9940
		Product-layer diffusion	0.0048	0.4254	0.9941
	Extended (8–54 h)	Surface reaction	0.0003	0.4724	0.9832
		Product-layer diffusion	0.0005	0.4586	0.9831
Ag	Global (2–54 h)	Surface reaction	0.0028	0.2599	0.7907
		Product-layer diffusion	0.0037	0.1689	0.8307
	Early (2–8 h)	Surface reaction	0.0168	0.1908	0.8642
		Product-layer diffusion	0.0195	0.0899	0.8856
	Extended (8–54 h)	Surface reaction	0.0017	0.3083	0.9770
		Product-layer diffusion	0.0024	0.2252	0.9806

Gold and silver were evaluated in parallel using identical regression windows to enable direct mechanistic comparison. Apparent rate constants (k), intercepts (C), and coefficients of determination (R²) derived from global, early-time, and extended-time SCM regressions are summarized in Table 10.

For gold, both surface-reaction-controlled and product-layer-diffusion-controlled SCM formulations exhibit comparable linear conformity across all

regression windows, with nearly identical R² values in the global regression. This behavior indicates that gold dissolution cannot be described by a single dominant rate-controlling mechanism. Instead, it proceeds under mixed kinetic control, involving concurrent surface chemical reaction and internal diffusional resistance.

During the early leaching stage (2–8 h), very high R² values (>0.99) and relatively large apparent rate constants are obtained for both SCM formulations. This response reflects rapid dissolution of readily accessible electrum and native Au–Ag alloy surfaces once cyanide and dissolved oxygen are available. Importantly, early-stage conformity to the surface-reaction SCM expression does not imply reagent limitation or intrinsic reaction control. Rather, it reflects a transient regime in which abundant reactive gold surface area is available and the surface reaction rate happens to be comparable to internal transport rates under reagent-sufficient conditions.

In the extended-time window (8–54 h), apparent rate constants decrease by nearly an order of magnitude, accompanied by systematic increases in intercept values. This evolution reflects a progressive decline in effective gold surface reactivity as readily accessible Au-bearing surfaces are depleted. Internal transport resistance associated with partial surface passivation, product-layer development, and micro-scale diffusional barriers becomes increasingly significant. The persistence of similar R² values for both SCM formulations confirms a smooth evolution within a mixed-control regime, rather than an abrupt mechanistic transition.

Silver exhibits a distinctly different SCM response. Across all regression windows, the product-layer diffusion formulation consistently provides equal or higher R² values than the surface-reaction formulation, particularly in the global and extended-time regressions. This behavior indicates that internal diffusional resistance constitutes the dominant kinetic constraint for silver dissolution.

Notably, even during the early leaching stage, diffusion-based SCM linearization provides superior conformity, indicating that silver does not exhibit a clearly defined surface-reaction-controlled regime. This response reflects the mineralogical deportment of silver in the Mount Muro low-sulphidation epithermal system, where a substantial fraction of Ag is hosted in sulfides and Cu–Ag sulfosalts. In these phases, dissolution is constrained by transport through partially oxidized surface layers, sulfur-rich reaction products, and fine-grained mineral matrices, in addition to intrinsic differences in cyanide complex stability relative to gold as shown in Table 11.

Higher intercept values and lower global R² values for silver further indicate persistent limitations in effective surface accessibility that are not alleviated solely by extended leaching time or continued reagent availability.

The SCM-based diagnosis demonstrates that gold and silver, despite their strong spatial association within electrum-bearing domains, dissolve under distinct dominant kinetic regimes. Gold dissolution evolves from initially rapid surface reaction on accessible

electrum surfaces toward increasing diffusional resistance as effective reactive area declines, whereas silver dissolution is diffusion-dominated from the onset of leaching.

Table 11. Mechanistic interpretation of SCM-based dissolution behavior for gold and silver

Aspect	Gold (Au)	Silver (Ag)
Dominant host phases	Electrum, native Au–Ag alloy	Electrum + Ag sulfides + Cu–Ag sulfosalts
Early-stage behavior	Rapid dissolution from exposed surfaces	No distinct reaction-controlled regime
Dominant SCM conformity	Mixed surface reaction + diffusion	Product-layer diffusion
Evolution with time	Progressive loss of reactive surface area	Persistent internal diffusion limitation
Key controlling factor	Declining accessibility	Sulfide/sulfosalt-controlled transport
Implication	Transition within mixed control	Diffusion-dominated throughout

These mechanistic distinctions are fully consistent with diagnostic leaching results (Section 3.1.4), residue characterization and size-based recovery behavior (Section 3.3), and time-resolved extraction trends (Section 3.2). Accordingly, the SCM analysis establishes a robust mechanistic foundation for the kinetic model discrimination presented in Section 3.4.2, where models capable of accommodating time-dependent loss of surface accessibility and internal diffusional resistance are shown to provide the most physically consistent representation of the observed cyanidation behavior.

3.4.2 Kinetic model fitting, discrimination, and geometallurgical relevance

Following the SCM-based mechanistic diagnosis, a suite of kinetic models integrating or conceptually consistent with the shrinking-core framework was evaluated to quantitatively describe the time-dependent dissolution behavior of gold and silver. Beyond statistical curve fitting, this analysis discriminates among kinetic models based on (i) predictive accuracy, (ii) physical consistency with the diagnosed rate-controlling behavior, and (iii) compatibility with the mineralogical and textural characteristics of the Mount Muro low-sulphidation epithermal (LSE) system.

As documented by Syaban et al. (2024)[9], Mount Muro mineralization is dominated by electrum and native Au–Ag alloys, with significant contributions from Ag sulfides (acanthite–argentite) and Cu–Ag sulfosalts (e.g., tetrahedrite–tennantite). These phases occur predominantly as fine inclusions, replacement textures, and disseminations within sulfide and gangue matrices. Such mineralogical architecture inherently promotes progressive loss of effective reactive surface area and the development of internal transport

constraints, rather than idealized single-mechanism kinetic behavior, even under reagent-sufficient cyanidation conditions.

To avoid over-reliance on correlation alone, particularly in non-linear leaching systems where high R^2 values may mask systematic misfit, model performance was evaluated using both goodness-of-fit (R^2) and error-based metrics (RMSE and MAE). Comparative results for gold and silver are summarized in Table 12.

Classical SCM formulations assuming pure surface-reaction control or pure product-layer diffusion control exhibit only moderate conformity ($R^2 \approx 0.79–0.84$). This behavior is consistent with their intended diagnostic role in identifying dominant resistances, but highlights their limited capacity to represent time-dependent decay in effective reactive surface area and heterogeneous mineral accessibility characteristic of LSE ores.

Table 12. Statistical performance of kinetic models for gold and silver dissolution

Gold (Au) Model	RMSE	MAE	R^2
Diffusion SCM	0.3629	0.3359	0.8403
Surface SCM	0.3517	0.3256	0.8396
Mintek	0.3700	0.3100	0.9998
KBK	0.3706	0.3088	0.9998
Crundwell	0.2283	0.1450	0.9999
Ling	0.0066	0.0058	0.99977
Loveday	0.2522	0.1994	0.9999
Silver (Ag) Model	RMSE	MAE	R^2
Diffusion SCM	0.3986	0.3687	0.8307
Surface SCM	0.3333	0.3075	0.7907
Mintek	1.6200	1.1800	0.9960
KBK	1.6177	1.1811	0.9960
Crundwell	0.7736	0.6041	0.9999
Ling	0.0307	0.0251	0.9977
Loveday	1.7948	1.2556	0.9951

Empirical formulations such as the Mintek and KBK models achieve very high R^2 values (>0.996 for both metals). However, their relatively large RMSE and MAE values indicate reduced precision in reproducing the full extraction trajectory. In the context of Mount Muro, this reflects the inability of purely empirical models to explicitly capture selective depletion of readily accessible electrum surfaces and the increasing dominance of sulfide- and sulfosalt-hosted Au–Ag domains documented through residue characterization and correlation analysis (Section 3.3).

The Crundwell model yields competitive R^2 values for both Au and Ag, reflecting its electrochemical basis and explicit coupling of metal dissolution with sulfide oxidation processes. This formulation is conceptually aligned with the presence of sulfide-associated Ag and Cu–Ag sulfosalts in the Mount Muro ore. Nevertheless, its substantially higher RMSE and MAE relative to the Ling model indicate systematic overprediction of late-stage reactivity, particularly where partial surface passivation, product-layer development, and internal diffusional barriers increasingly constrain dissolution.

By contrast, the Ling model consistently provides the lowest prediction errors for both gold and silver while maintaining high correlation with experimental data. This superior performance reflects its ability to

represent non-linear, accessibility-controlled kinetics arising from progressive loss of effective Au–Ag surface reactivity, rather than from limitations in reagent availability or intrinsic reaction feasibility. Importantly, this behavior is fully consistent with the mixed-control dissolution of gold and diffusion-dominated dissolution of silver diagnosed through SCM linearization in Section 3.4.1.

3.4.3 Optimized Ling rate expressions and physical meaning of parameters

The optimized Ling-model rate expressions obtained in this study are shown in Eq. (6) and (7):

$$-\frac{d[Au]_p}{dt} = 0.008679 [CN^-]^{1.0239} [O_2]^{0.2519} ([Au]_p - 0.1985)^{1.6354} \quad (6)$$

$$-\frac{d[Ag]_p}{dt} = 0.002745 [CN^-]^{0.7970} [O_2]^{0.2918} ([Ag]_p - 0.5402)^{2.0901} \quad (7)$$

where $[Au]_p$ and $[Ag]_p$ represent the remaining solid-phase fractions of gold and silver, respectively.

The elevated apparent reaction orders with respect to residual metal concentration ($\alpha = 1.64$ for Au; $\alpha = 2.09$ for Ag) deviate significantly from ideal SCM values (≈ 0.66 – 1.0). This deviation reflects non-ideal surface conditions associated with mineralogical heterogeneity, partial passivation, and micro-scale diffusional barriers, rather than any limitation in chemical reaction feasibility. These interpretations are fully consistent with residue characterization (Section 3.3) and the SCM-based mechanistic diagnosis (Section 3.4.1).

The near-first-order dependence on cyanide ($\beta \approx 0.8$ – 1.0) confirms that cyanide availability remains kinetically relevant under reagent-sufficient conditions, while the low reaction order with respect to dissolved oxygen ($\gamma \approx 0.25$ – 0.29) demonstrates that oxygen transfer is not rate-limiting. Oxygen acts instead as a secondary facilitator of surface conditioning rather than a primary kinetic driver. The accurate prediction of the terminal gold residue concentration further supports the existence of mineralogically constrained Au fractions that are chemically inaccessible without additional physical or chemical modification.

3.5 Integrated kinetic–mineralogical synthesis and geometallurgical implications

An integrated synthesis of mineralogical characterization, diagnostic leaching, residue analysis, and kinetic modeling provides a coherent and mechanistically consistent explanation for the contrasting cyanidation behavior of gold (Au) and silver (Ag) in the Mount Muro low-sulphidation epithermal (LSE) ore. Although Au and Ag are strongly spatially associated, predominantly as electrum and native Au–Ag alloys, their dissolution trajectories diverge markedly once leaching commences. This divergence does not reflect differences in chemical feasibility or reagent sufficiency, but instead arises from fundamental

contrasts in mineralogical hosting, thermodynamic competition during oxidation, and the progressive evolution of effective surface accessibility during leaching.

From a mineralogical standpoint, the key asymmetry lies in the structural role of sulfides and sulfosalts. Gold does not form independent Au–sulfide phases; its occurrence within sulfides is minor, dispersive, or substitutional, and Au is not structurally bound to Cu-bearing minerals. As a result, most Au is liberated or semi-exposed once electrum-bearing domains are intersected by grinding. Silver, by contrast, frequently occurs as discrete Ag sulfides (acanthite–argentite) and as a structural constituent of Cu–Ag sulfosalts (e.g., tetrahedrite–tennantite), in addition to its presence in electrum. These phases impose intrinsic crystallographic and chemical constraints that persist even at fine particle sizes.

The Mount Muro ore, dissolved oxygen preferentially reacts with sulfide and sulfosalts phases, processes that are strongly favored energetically, before participating in the oxidative dissolution of metallic Ag. For Ag hosted within sulfides or sulfosalts, oxygen is therefore diverted toward surface oxidation reactions that generate elemental sulfur, metal oxyhydroxides, or mixed product layers. While such oxidation can locally disrupt mineral lattices, it simultaneously promotes surface passivation and increases internal diffusional resistance. Gold is far less affected by this competition because it is not structurally incorporated within sulfide lattices; initial sulfide oxidation may even transiently enhance Au exposure before passivation becomes dominant.

These thermodynamic tendencies are expressed dynamically in the observed kinetics. SCM-based diagnosis demonstrates that gold dissolution evolves under mixed kinetic control. During early leaching, when abundant electrum and native Au–Ag surfaces are exposed, dissolution appears surface-reaction-dominated, not because diffusion is negligible, but because the intrinsic electrochemical reaction proceeds at a rate comparable to, and temporarily slower than, mass transport under these conditions. As leaching progresses, accessible Au surfaces are progressively depleted, and internal diffusion through partially passivated layers increasingly constrains the rate. This evolution is smooth and continuous, with no abrupt mechanistic transition.

Silver exhibits a fundamentally different response. SCM linearization shows that Ag dissolution is diffusion-dominated from the onset of leaching. Even at early times, silver does not exhibit a clear surface-reaction-controlled regime, reflecting its strong association with sulfide and Cu–Ag sulfosalts matrices. In these domains, dissolution is limited by transport through oxidized surface layers and fine-grained mineral frameworks, compounded by the lower thermodynamic stability and slower intrinsic kinetics of the $Ag(CN)_2^-$ complex relative to $Au(CN)_2^-$.

Residue characterization and correlation analysis provide direct physical evidence for this mechanistic divergence. Selective depletion of electrum during leaching leads to a systematic shift from strong Au–Ag

association in the feed toward enhanced Au–Cu and Ag–Cu coupling in the residue, indicating preferential retention of precious metals within refractory sulfide and sulfosalt domains. Importantly, unrecovered Au and Ag are concentrated in the finest size fractions, demonstrating that residual losses are not governed by coarse-particle shielding or insufficient comminution, but by mineralogical and surface-related accessibility constraints.

Table 13. Integrated mineralogical–thermodynamic–kinetic framework explaining contrasting Au and Ag cyanidation behavior in the Mount Muro LSE system

Aspect	Gold (Au)	Silver (Ag)	Mechanistic implication
Primary host phases	Native Au, electrum	Electrum + Ag sulfides + Cu–Ag sulfosalts	Structural freedom vs lattice-bound behavior
Structural relation to sulfides	Not structurally bound	Frequently structurally bound	Governs need for lattice disruption
Initial cyanide accessibility	Predominantly free-milling	Partially sulfide- and sulfosalt-hosted	Defines initial accessibility contrast
Thermodynamic competition for O ₂	Weak	Strong	O ₂ diverted toward sulfide oxidation for Ag
Effect of sulfide oxidation	Transient exposure, later passivation	Predominantly passivating	Opening vs persistent inhibition
Early kinetic regime	Apparent surface-reaction dominance	Diffusion-dominated	Reflects surface availability
Kinetic evolution	Mixed control with time	Diffusion-controlled throughout	Progressive accessibility loss
SCM diagnostic outcome	Mixed control	Product-layer diffusion	Distinct dominant resistances
Residue correlation shift	Au increasingly correlated with Cu	Strong Ag–Cu coupling	Retention in refractory domains
Best kinetic framework	Ling model	Ling model	Accessibility-controlled kinetics
Dominant cause of losses	Surface passivation	Structural sulfide/sulfosalt binding	Not reagent- or time-limited
Response to finer grinding	Diminishing returns	Limited benefit	Chemical constraints dominate
Geometallurgical implication	Mildly constrained free-milling	Mildly refractory behavior	Different process levers required

Within this context, kinetic model discrimination confirms that a single idealized rate-controlling mechanism cannot adequately describe the system. Classical SCM formulations capture diagnostic trends but lack the flexibility to represent time-dependent decay in effective reactive surface area.

Empirical models achieve high correlation but obscure physical meaning. The Ling model, by contrast, provides a unified framework capable of accommodating non-linear, accessibility-controlled kinetics for both Au and Ag. Elevated apparent reaction orders with respect to residual metal concentration encode progressive surface passivation and loss of effective reactive area, while near-first-order dependence on cyanide and weak oxygen sensitivity confirm that reagent availability and redox conditions are not rate-limiting under the applied conditions. The integrated mechanistic framework developed here is summarized schematically in Table 13, which contrasts gold and silver behavior across mineralogical, thermodynamic, kinetic, and operational dimensions.

From a geometallurgical perspective, this synthesis demonstrates that extending leaching time or increasing reagent dosage alone is unlikely to yield substantial additional recovery. Further grinding beyond the applied P₈₀ similarly offers diminishing returns, as residual Au and Ag already reside in fine, mineralogically constrained domains. Improving recovery, particularly for silver, requires strategies that directly modify sulfide and sulfosalt accessibility, such as targeted pre-oxidation or alternative flowsheets, rather than conventional cyanidation optimization.

Overall, the Mount Muro case illustrates that Au and Ag dissolution in LSE systems can be reconciled within a common kinetic framework while remaining governed by distinct dominant mechanisms. The shared applicability of the Ling model reflects a common control by evolving surface accessibility, whereas contrasting parameter values encode mineralogically driven differences in dissolution behavior. This integrated mineralogical–thermodynamic–kinetic approach provides a robust foundation for translating laboratory cyanidation data into mechanistic understanding and realistic geometallurgical decision-making.

4 Conclusions

This study demonstrates that the cyanidation behavior of gold (Au) and silver (Ag) in the Mount Muro low-sulfidation epithermal (LSE) system is governed primarily by mineralogical constraints rather than reagent availability. Diagnostic leaching established that >85% of gold is cyanide-amenable at the applied grind size (P₈₀ ≈ 75 μm), whereas only ~55% of silver is readily accessible, with the remainder hosted in sulfide and Cu–Ag sulfosalt phases. Continuous cyanidation confirmed this contrast: gold achieved 92% recovery within 24 h, while silver extraction plateaued at ~68% after 54 h. Residue characterization revealed that unrecovered Au and Ag were concentrated in fine fractions (<38 μm), indicating that incomplete recovery

is controlled by mineralogical locking, partial passivation, and micro-scale diffusional barriers rather than coarse-particle shielding.

Kinetic analysis using Shrinking Core Model (SCM) linearization identified mixed control for gold and diffusion-dominated control for silver. Model discrimination further showed that, despite differing mechanisms, both metals are best represented by the Ling model, which yielded the lowest prediction errors (RMSE = 0.0066, MAE = 0.0058 for Au; RMSE = 0.0307, MAE = 0.0251 for Ag) while maintaining high correlation ($R^2 > 0.99$). Optimized parameters highlight that dissolution rates are controlled by progressive loss of effective surface accessibility due to mineralogical heterogeneity and product-layer development.

From a geometallurgical perspective, extending leaching time or increasing reagent dosage is unlikely to substantially improve recovery. Instead, strategies targeting sulfide and sulfosalt accessibility, such as pre-oxidation or alternative processing routes, are required to enhance silver extraction. Overall, this integrated mineralogical–kinetic approach provides a physically consistent framework for interpreting cyanidation behavior in mildly refractory LSE ores and informs realistic process design for complex epithermal systems.

References

- [1] J. R. . Craig and D. J. . Vaughan, *Ore microscopy and ore petrography*. Wiley, 1994.
- [2] S. R. La Brooy, H. G. Linge, and G. S. Walker, “Review of gold extraction from ores,” *Miner. Eng.*, vol. **7**, no. 10, pp. 1213–1241, Oct. 1994, doi: 10.1016/0892-6875(94)90114-7.
- [3] N. C. WHITE and J. W. HEDENQUIST, “Epithermal Gold Deposits: STYLES, CHARACTERISTICS AND EXPLORATION,” *SEG Discovery*, no. **23**, pp. 1–13, Oct. 1995, doi: 10.5382/SEGnews.1995-23.fea.
- [4] J. Hedenquist, A. Arribas, and E. Gonzalez-Urien, “Exploration for Epithermal Gold Deposits,” *Reviews in Economic Geology*, vol. **13**, pp. 245–277, Jan. 2000.
- [5] G. J. . Corbett and T. M. . Leach, *Southwest pacific rim gold-copper systems : structure, alteration, and mineralization*. Society of Economic Geologists, 1998.
- [6] N. J. Cook, C. L. Ciobanu, and J. Mao, “Textural control on gold distribution in As-free pyrite from the Dongping, Huangtuliang and Hougou gold deposits, North China Craton (Hebei Province, China),” *Chem. Geol.*, vol. **264**, no. 1–4, pp. 101–121, Jun. 2009, doi: 10.1016/J.CHEMGEO.2009.02.020.
- [7] S. C. Dominy, L. O’Connor, A. Parbhakar-Fox, H. J. Glass, and S. Purevgerel, “Geometallurgy—A Route to More Resilient Mine Operations,” *Minerals*, vol. **8**, no. 12, p. 560, Dec. 2018, doi: 10.3390/min8120560.
- [8] V. Lishchuk, P.-H. Koch, Y. Ghorbani, and A. R. Butcher, “Towards integrated geometallurgical approach: Critical review of current practices and future trends,” *Miner. Eng.*, vol. **145**, p. 106072, Jan. 2020, doi: 10.1016/j.mineng.2019.106072.
- [9] S. N. Syaban, A. Idrus, L. D. Setijadji, and I. Setiawan, “Hydrothermal Alteration, Ore Mineralization, and Fluid Inclusions Study of the Mount Muro Low Sulphidation Epithermal Deposit, Murung Raya Regency, Central Kalimantan Province, Indonesia,” *IOP Conf. Ser. Earth Environ. Sci.*, vol. **1378**, no. 1, p. 012028, Jul. 2024, doi: 10.1088/1755-1315/1378/1/012028.
- [10] S. F. Simmons and P. R. L. Browne, “Mineralogic, alteration and fluid-inclusion studies of epithermal gold-bearing veins at the Mt. Muro Prospect, Central Kalimantan (Borneo), Indonesia,” *J. Geochem. Explor.*, vol. **35**, no. 1–3, pp. 63–103, Jan. 1990, doi: 10.1016/0375-6742(90)90036-A.
- [11] A. T. Wurst, “Geology and genesis of the Permata-Batu Badinding-Hulubai and Kerikil Au-Ag low sulfidation epithermal deposits, Mt Muro, Kalimantan, Indonesia,” UNIVERSITY OF TASMANIA, 2004.
- [12] F. K. Crundwell and S. A. Godorr, “A mathematical model of the leaching of gold in cyanide solutions,” *Hydrometallurgy*, vol. **44**, no. 1, pp. 147–162, 1997, doi: [https://doi.org/10.1016/S0304-386X\(96\)00039-4](https://doi.org/10.1016/S0304-386X(96)00039-4).
- [13] P. Ling, V. G. Papangelakis, S. A. Argyropoulos, and P. D. Kondos, “AN IMPROVED RATE EQUATION FOR CYANIDATION OF A GOLD ORE,” 1996.
- [14] O. Levenspiel, “Chemical Reaction Engineering,” *Ind. Eng. Chem. Res.*, vol. **38**, no. 11, pp. 4140–4143, Nov. 1999, doi: 10.1021/ie990488g.
- [15] Michael. Nicol, N. J. . Welham, and Gamini. Senanayake, *Hydrometallurgy. Volume 2, Practice*. Elsevier, 2022.